Photoacoustics 28 (2022) 100410

Contents lists available at ScienceDirect

Photoacoustics

journal homepage: www.elsevier.com/locate/pacs

In vivo quantitative photoacoustic evaluation of the liver and kidney pathology in tyrosinemia

Guojia Huang [a,1], Jing Lv [a,b,c,1], Yong He [d], Jian Yang [e], Lvming Zeng [d,*], Liming Nie [a,f,**]

[a] Research Center of Medical Sciences, Guangdong Provincial People's Hospital, Guangdong Academy of Medical Sciences, 510000 Guangzhou, China
[b] Guangdong Cardiovsacular Institute, 510000 Guangzhou, China
[c] School of Public Health, Xiamen University, 361005 Xiamen, China
[d] State Key Laboratory of Precision Electronic Manufacturing Technology and Equipment, Guangdong University of Technology, 510000 Guangzhou, China
[e] Department of Hepatobiliary Surgery, Zhujiang Hospital, Southern Medical University, 510000 Guangzhou, China
[f] Guangdong Provincial Key Laboratory of Artificial Intelligence in Medical Image Analysis and Application, Guangdong Provincial People's Hospital, Guangdong Academy of Medical Sciences, 510000 Guangzhou, China

ARTICLE INFO

Keywords:
Photoacoustic imaging
Tyrosinemia
Hepatic lobule
Renal tubule

ABSTRACT

Hereditary tyrosinemia type I (HT1) is a severe autosomal recessive inherited metabolic disease, which can result in severe damage of liver and kidney. Photoacoustic imaging (PAI) uses pulsed laser light to induce ultrasonic signals to facilitate the visualization of lesions that are strongly related to disease progression. In this study, the structural and functional changes of liver and kidney in HT1 was investigated by cross-scale PAI. The results showed that the hepatic lobule and renal tubule were severely damaged during HT1 progression. The hemoglobin content, vessel density, and liver function reserve were decreased. The metabolic half-life of indocyanine green declined from 59.8 s in health to 262.6 s in the advanced stage. Blood oxygen saturation was much lower than that in health. This study highlights the potential of PAI for in vivo evaluation of the liver and kidney lesions in HT1.

1. Introduction

Hereditary tyrosinemia type-1 (HT1) is a autosomal recessive inherent error of metabolism caused by the deficiency of fumarylacetoacetate hydrolase (FAH) [1]. The FAH enzyme mainly in the liver and kidney catalyzes the last step of tyrosine metabolism [2,3]. Metabolic block of the step of FAH induces accumulation of toxic metabolites and further results in severe liver damage, nodular liver cirrhosis, renal tubular defects, and risk of hepatocellular carcinoma [4–6]. Survivors of these devastating complications often transitioned to hepatocellular carcinoma with lifetime frequencies as high as 37 % [7,8]. Variable degree of renal dysfunction ranges from mild tubular dysfunction to chronic renal disease, and the characteristic renal disease is a tubular disorder [9]. HT1 is a rare disease that occurs worldwide with an incidence of 1/120,000–1/100,000 [1]. In the absence of treatment, most patients with HT1 die of acute severe liver and kidney failure in early infancy [10]. Therefore, it is of great significance to further detailedly examine the liver and kidney lesions in HT1.

Clinical manifestations and special laboratory tests are the routine clinical examination for the diagnosis of HT1, and gene mutation analysis is the gold standard of definite diagnosis [11]. FAH activity and liver nodules are the two important diagnostic indexes. FAH activity has been measured in liver biopsy specimens. Since reversion of mutations in one allele of the FAH gene might take place and lead to mosaicism, enzyme determinations from liver tissue can be usually misleading and results in normal hepatic enzyme levels [10,12]. Multiple nodules in the liver parenchyma are typical for HT1. Biopsy of small nodule (less than 1 cm) is fraught with problems such as inadequate tissue or sampling errors. Furthermore, these nodules are not easily distinguishable from tumors [13].

Imaging studies are important and visual for evaluating and monitoring the pathophysiological state in HT1. Current guidelines

* Corresponding author.
** Corresponding author at: Research Center of Medical Sciences, Guangdong Provincial People's Hospital, Guangdong Academy of Medical Sciences, 510000 Guangzhou, China.
E-mail addresses: zenglvming@163.com (L. Zeng), limingnie@gmail.com (L. Nie).
[1] These authors contributed equally.

https://doi.org/10.1016/j.pacs.2022.100410
Received 24 June 2022; Received in revised form 9 September 2022; Accepted 27 September 2022
Available online 28 September 2022

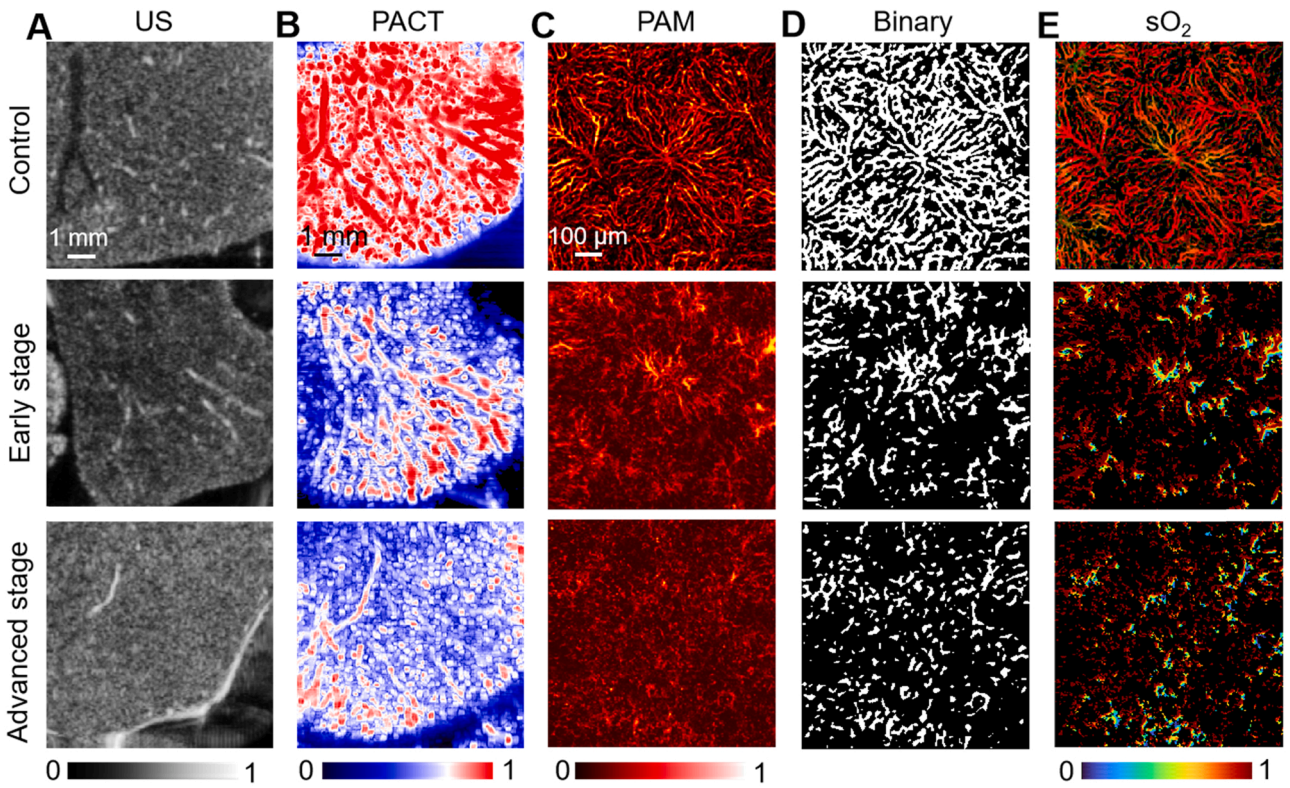

Fig. 1. Transverse US and PA images of mouse liver at different stages of modeling. A–C, Transverse US, PACT, PAM images of mouse liver. D, Filter and binary processing of PAM image. E, sO_2 of mouse liver.

encourage that single abdominal ultrasound (US) can detect nodules larger than 2 mm in diameter, and renal US can also observe the changes of renal structure, such as renal enlargement and tubule dilatation [14]. Magnetic resonance imaging (MRI) is more helpful than CT for detection and characterization of the sub centimeter liver nodules, and is the most reliable technique to evaluate liver lesions in HT1 patients [15]. However, the sensitivity of MRI is reduced to 33–67 % for nodules less than 1 cm in cirrhosis, while the sensitivity is 58.5–93 % for nodules larger than 1 cm [16]. Furthermore, these imaging techniques are still insufficient in terms of the microstructure and blood oxygen function of liver and kidney.

Photoacoustic (PA) imaging (PAI) is currently one of the most promising non-invasive biomedical imaging techniques [17,18]. Unlike the conventional clinic techniques, PAI provides the optical absorption differences of molecules including endogenous absorption group [19], and exogenous contrast agent [20]. The endogenous contrast reveals the histological, anatomical, functional and metabolic properties of tissue, while the exogenous contrast can provide molecular and cellular specificity [21,22]. The absorption spectra obtained with PAI can be analyzed by applying spectral unmixing, allowing the extraction of molecular information such as oxyhemoglobin and deoxyhemoglobin to rapidly obtain the microvascular structure information and blood oxygen saturation (sO_2) [23]. With the help of exogenous probes, PAI can selectively detect specific molecular markers with high sensitivity [24,25]. So far, PAI has been used in preclinical study [26], with major potential for clinical applications in the future [27]. Generally, subjected to different methods of optical illumination and acoustic detection, PAI systems can be grouped into computed tomography (or tomography), mesoscopy and microscopy systems [21,28]. The spatial resolution of photoacoustic computed tomography (PACT) scales with the imaging depth over wide range from the quasi-ballistic regime (typically $\leq$1 mm in tissue) to the diffusive regime (typically $\geq$ 10 mm in tissue), up to the dissipation limit ($\sim$ 10 cm in tissue) [29]. Photoacoustic microscopy (PAM) enables organelle and cellular level imaging from its high lateral resolution spanning hundreds of nanometer to several micrometers [30]. The spatial scale of PAI covers organelles, cell, tissues, organs, and small animals [31]. Thus, PAI has great potential to examine the microstructural and functional change in HT1.

In recent years, PAI has been widely used for the diagnosis and treatment of liver and renal disease [32,33]. (1) PAI mediated diagnosis of liver and renal diseases. Biopsy-free assessment of hepatic Cu via PAI was successfully identified Wilson's disease from healthy group [34]. Drug-induced liver injury [35], small hepatocellular carcinoma detection [36] and visualization of peroxisomal viscosity in non-alcoholic fatty liver [37] were also performed by PAI. Collagen, the principal component of fibrotic tissue in kidney has been mapped for assessing pretransplant organ quality by PAI [38]. (2) PAI evaluation of liver and kidney function. Real-time PACT system was proposed to in vivo non-invasively access liver function reserve based on indocyanine green (ICG) concentration change [39]. With the aid of ultra-small black phosphorous quantum dots, PAI was applied to evaluate the clearance function of acute kidney injury and chronic kidney disease, and has higher detection sensitivity than the clinical serum indices examination method [40]. (3) PAI guidance of therapy and surgery. With the help of Au@liposome-ICG), PAI shows effective guidance from tumor detection to surgery guidance in orthotopic liver cancer mouse models [41].

In previous work, our research group has carried out a series of studies on the diagnosis of liver diseases by PAI. The metabolic capacity evaluation model was established to dynamically monitor the circulatory dynamics of ICG in real time, and to evaluate the metabolic capacity of fibrosis liver at different stages by dynamic contrast-enhanced PAI [42]. The precise location and size of early hepatic micrometastases were determined at the submillimeter level [43]. Furthermore, a new method of PAI guided photothermal ablation under laparoscopic guidance was proposed to ablate orthotopic hepatocellular carcinoma [44]. To our knowledge, visualization of microscopic pathological features of liver and kidney in HT is rarely reported, which impelled us to further investigate the lesion characteristics of HT1 taking the special

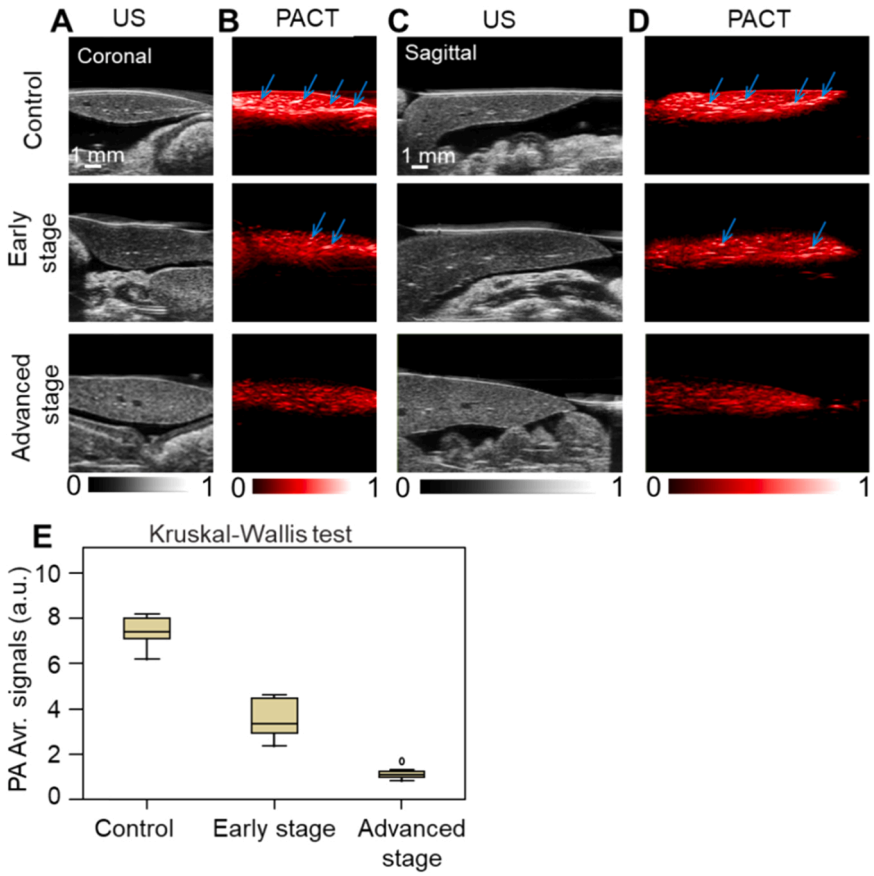

Fig. 2. US and PACT images of mouse liver in the coronal and sagittal plane. A, Coronal US images. B, Coronal PACT images. C, Sagittal US images. D, Sagittal PACT images. Arrow indicates the cross section of the blood vessel. E, Quantification of PA average signals of mouse liver. a.u. = arbitrary units, Avr. = average.

advantages of PAI.

The purpose of this work is to show the feasibility of PAI to obtain the microstructural information and functional parameters of the liver and kidney in mouse model of HT1. The morphology of liver and kidney was presented by an integrated US and PACT system. The microvascular structure and sO_2 were obtained by PAM. Furthermore, the assessment of liver function reserve and hemoglobin content was performed. The results can promise to provide new reference methods for HT1 diagnosis and monitoring with high spatial imaging resolution.

2. Materials and methods

2.1. Photoacoustic imaging system

PACT was performed using a Vevo LAZR-X instrument (Vevo, Fujifilm Visual Sonics), where a laser excitation source (680–950 nm) generates a pulse of light every 0.2 s via optical fibers. The acoustic signal is measured with an linear US transducer operating at a central frequency of 40 MHz.

PAM was carried out by a commercial convertible optical and acoustic resolution PAM instrument (G2, Inno Laser), equipped with series of 532 nm, 559 nm, 750–840 nm multi-wavelength lasers. The central frequency of US transducer is 50 MHz, providing an optical resolution of 5 μm and an acoustic resolution of 40 μm.

2.2. Disease models

The research complied with Laboratory Animal Center standards for the care and use of laboratory animals. All experiments were approved by the Animal Research Ethics Committee and were performed by relevant guidelines and regulations. FAH heterozygous gene (FAH+/-) ICR mice (body weight range, 25–30 g) were purchased from Xiamen University used for breeding. On the feeding conditions: 12 h light/12 h dark rhythm, all animals were fed with standard feed and water. Knockout (FAH-/-) mice (n = 28) and healthy (FAH+/+ or FAH+/-) mice (n = 14) were obtained.

2.3. Experimental procedure

2.3.1. US and PACT imaging of liver and kidneys

During the experiments, the mouse was anesthetized with 2 % isoflurane. Firstly, the hair on the abdomen was removed and then fixed on the imaging platform. Three-dimensional PA images of whole-liver and kidney were acquired at 680 nm, as the absorption signals of hemoglobin in blood were relatively strong under this wavelength. The scanning step size was 0.08 mm. After that, the mean value of PA signals in each B-scan frame was calculated by using the image processing software of the PAI system, and then the sum of the PA signals was obtained. The final average value of the PA signal was obtained by dividing the total number of B-scan frames.

2.3.2. Liver function reserve

An indwelling needle was inserted into the tail vein, and then 0.3 mL (3 mmol per kilogram of body weight) of ICG solution was injected at a constant rate of 0.1 mL/s. PACT scan at 800 nm (absorption peak of ICG in the blood) was performed, and the PA signal was continuously acquired for additional 5 min after the injection of ICG. The control group was injected with 0.9 % physiologic saline.

2.3.3. PAM imaging of liver and kidneys

Mice were anesthetized with 2 % isoflurane. A small laparotomy was performed to expose the liver lobe, while the kidneys were exposed after

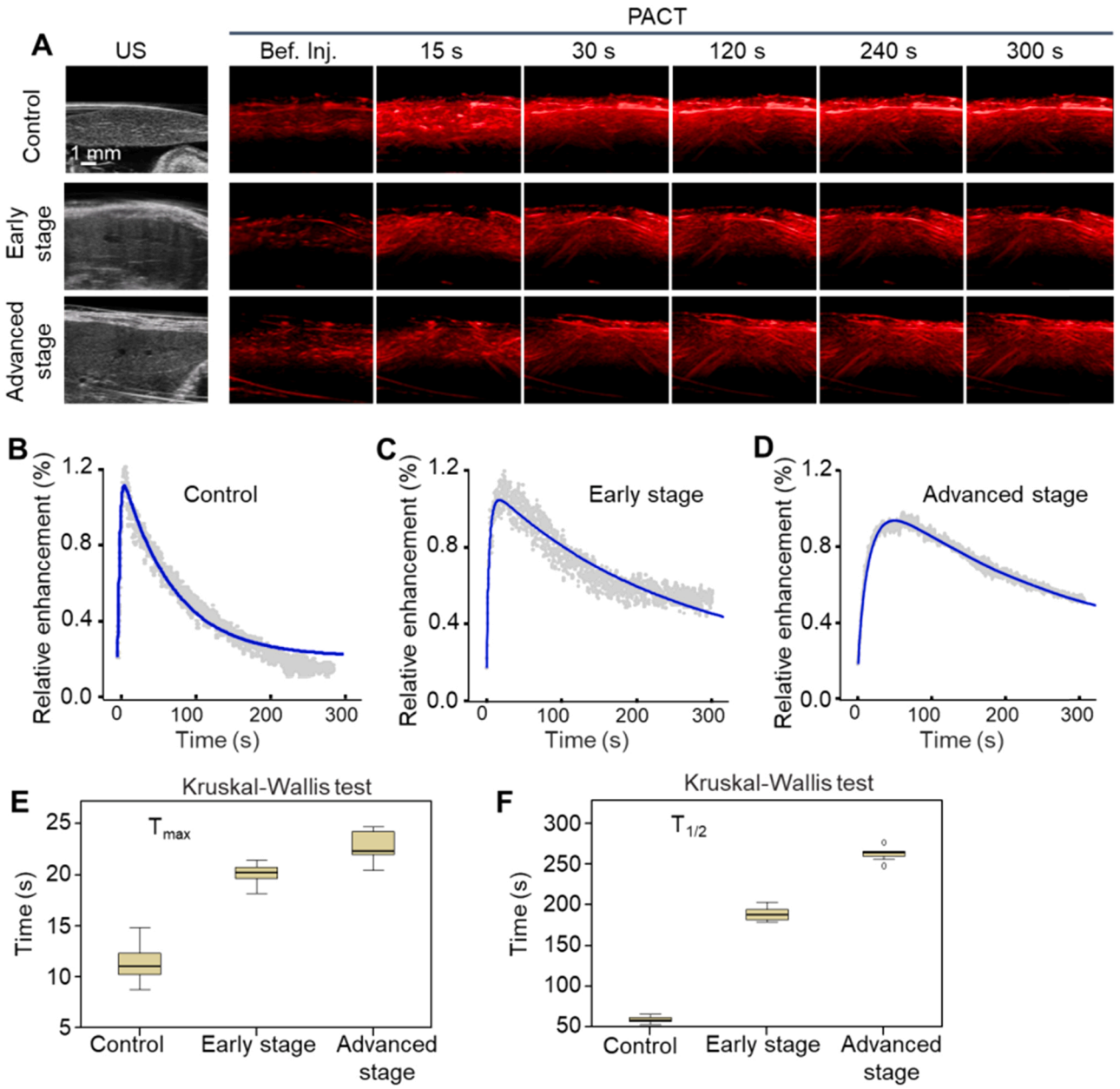

Fig. 3. Time course of ICG clearance studies by PACT. A, PA imaging of mouse liver before (Bef.) and after injection of ICG. B–D, Relative enhancement of liver function curves in the healthy, early and advanced stage of modeling, respectively. E, F, Quantitative T_{max} and $T_{1/2}$, respectively.

a small incision on the side of the spine. Structural and functional information on liver and renal surface was acquired under dual-wavelength (532 nm and 559 nm). The scanning range was 0.9 × 0.9 mm^2 with a step of 3 μm. The percentage of blood vessel area was calculated by dividing the total observed area.

2.4. Data analysis

The PA spectra were recorded and saved in the Vevo Lab software for the subsequent spectral unmixing and deconvolution. The self-written MATLAB R2021 b (Mathworks Inc. South Natick, MA, USA) program was used for image processing, such as structural imaging, calculation of blood vessel density and sO_2. Blood vessel density (BVD) reflects the amount of blood vessel distribution in a given region, and it is defined as:

$$\mathrm{BVD} = \text{Total vessel } \textit{length}/\text{Observed } \textit{volume} \quad (1)$$

where observed volume (mm^2) is the volume of the region under interest, and total vessel length (mm) is the accumulated length of all the measured blood vessels in this region. sO_2 mapping was calculated as follows [45]:

$$sO_2 = HbO_2/(HbO_2 + HbR) \quad (2)$$

PA signal intensity (SI) was measured for each PA image. Relative enhancement (RE) of SI was calculated using Eqs. (3) and (4):

$$RE(t) = ([SI(t) - SI(0)]/[SI(0)] \quad (3)$$

where SI(0) is the average SI before injection of ICG, SI(t) is the time course SI after injection. The time course of liver RE to reflect the change of ICG concentration was fitted using an mathematical method [46].

$$RE(t) = \left\{ \begin{matrix} 0 & , t < t_0 \\ A[1 - e^{-\alpha(t-t_0)}]^q * e^{-\beta(t-t_0)}, & \&t \geq t_0 \end{matrix} \right\} \quad (4)$$

Where A is the maximum value of the RE, α is the rate of contrast uptake

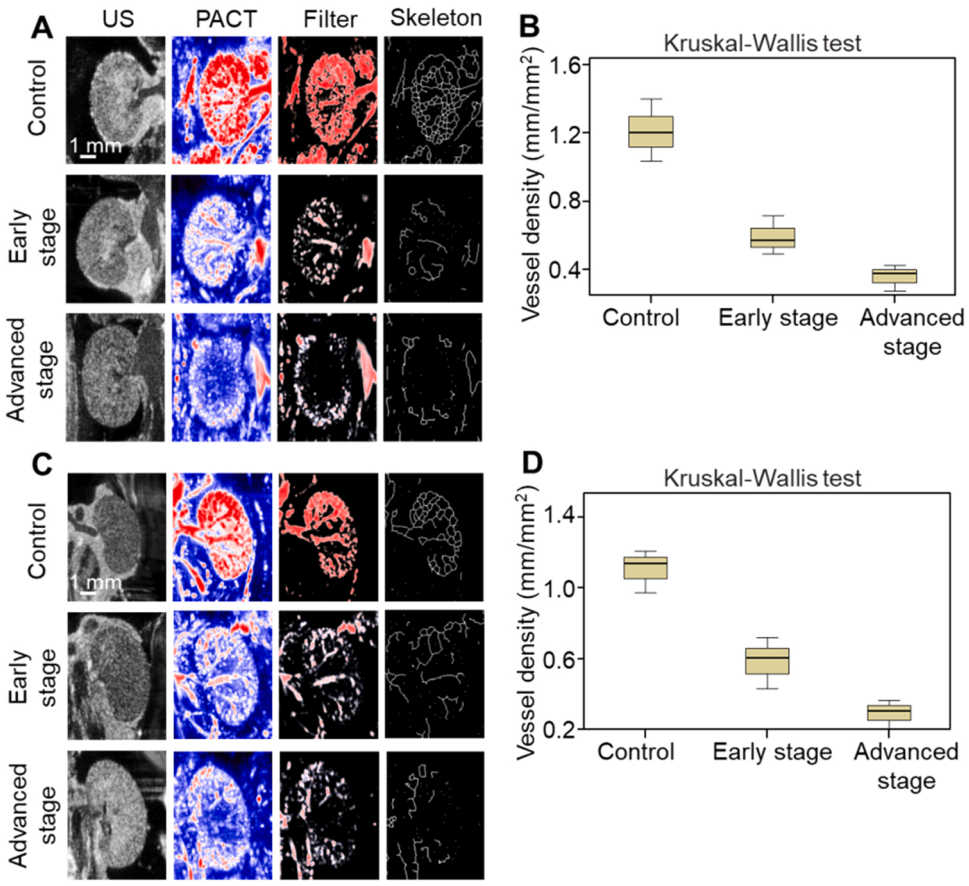

Fig. 4. Transverse US and PACT images of mouse kidneys at different stages of modeling. A, US and PACT images of left kidney. B, Quantification of the vessel density of left kidney. C, US and PACT images of right kidney. D, Quantification of the vessel density of right kidney.

(s^{-1}), β is the rate of contrast washout (s^{-1}), q is a parameter related to the slope of the early uptake, and t_0 is the rise time point (s). The maximum peak time T_{max} of RE and the half life period $T_{1/2}$ of the elimination RE were calculated from the fitted curve.

SPSS software (IBM 22) was used for statistical analysis. Statistical differences among groups were determined by using the Kruskal-Wallis test followed by the Kruskal-Wallis one-way analysis of variance (k samples) test for multiple comparisons. A p-value < 0.05 was considered significant.

For the image binaryzation, the algorithm was based on Matlab software to extract the vascular morphological features as previous report [47]. Firstly, the original MAP PA image was filtered and enhanced to obtain the best contrast, and the false negative pixels were removed. Then, the blood vessels were segmented by threshold processing and image binaryzation was performed. All the images share the same threshold of 0.3. Vessel density was calculated as the ratio of the number of pixels occupied by the vessels to the total number of pixels.

3. Results

3.1. Three-dimensional US and PAI of liver

Compared with healthy mice, transverse US images showed progressive nodular changes in liver parenchyma in HT1, accompanied by blunting of liver margins and loss of intrahepatic luminal structures as disease progressed (Fig. 1A). Transverse PACT images (Fig. 1B) exhibited that under healthy conditions, the vascular structure of the liver surface was continuous. In HT1 state, the vascular structure was damaged and blurred in the early stages, and became more severe in the advanced stages. PAM images (Fig. 1C) shows that the overall structure of the hepatic lobule, the smallest unit on the liver surface, is polygonal on the transverse plane as indicated in the healthy state. One side of the hepatic sinus was connected with the portal vein and hepatic artery, and the other side was connected with the central vein. The hepatic sinuses radiate around the central vein. However, in the disease model, the liver surface structure was no longer complete. The hepatic sinuses were discontinuous and gradually disappeared. The lobules are destroyed and the their microstructure could not be distinguished in severe cases. To better quantify the structural changes in hepatic lobule, the binarization of Fig. 1C was performed to obtain the images in Fig. 1D. The results showed the percentage of blood vessel area decreased gradually with disease progression (control group, 47.7 %; early stage, 23.8 %; advanced stage, 16.9 %), indicating the vascular network was severely damaged in HT1. Changes of sO_2 were measured to better assess the changes of hepatic lobule function (Fig. 1E). The quantitative results displayed that the sO_2 of mice in HT1 was significantly lower than that of normal healthy group (control group, 0.91; early stage, 0.83; advanced stage, 0.70), revealing that the decrease of sO_2 occurred simultaneously with the destruction of the vascular structure.

Fig. 2 shows the US and PACT images of the mouse liver in the coronal and sagittal plane, respectively. There were no significant differences in the vascular microstructure between the control group and disease groups in US images (Fig. 2A, C). Both from the coronal and sagittal sections, PACT demonstrated that the hemoglobin content decreased gradually as tyrosinemia worsened (Fig. 2B, D). The number of identifiable blood vessels in the liver is also reduced as indicated by the arrows. Fig. 2E shows the PA signals of total hemoglobin also declined (control group, 6.9 ± 1.5 a.u.; early stage, 2.8 ± 0.5 a.u.; advanced stage, 1.2 ± 0.4 a.u.; $P < 0.05$).

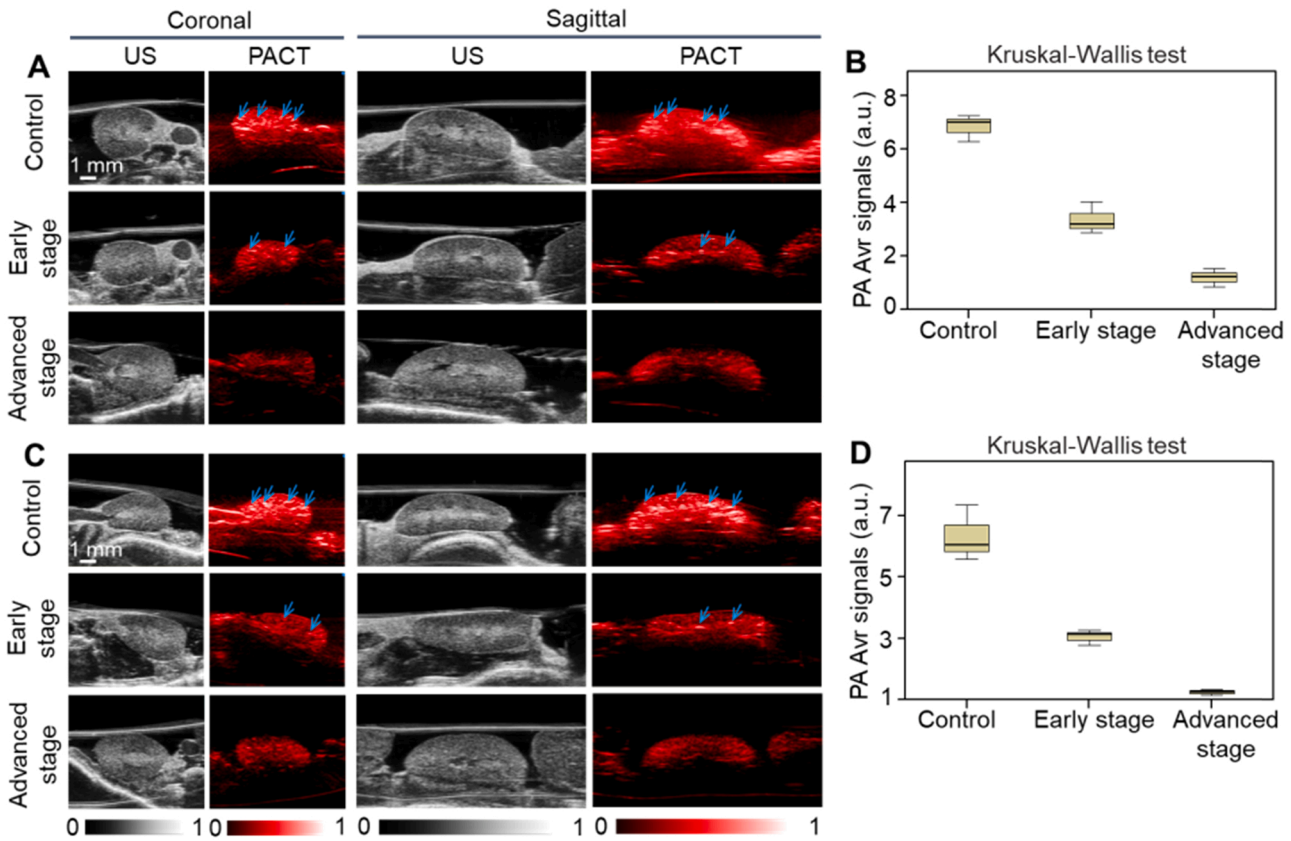

Fig. 5. US and PACT images of mouse kidneys in the coronal and sagittal plane. A, US and PACT images of left kidney. B, Quantitative PA average signals of left kidney. C, US and PA images of right kidney. D, Quantitative PA average signals of right kidney. Arrows indicate the hemoglobin signal. a.u. = arbitrary units, Avr. = average.

3.2. PACT measurement of liver function reserve

Time course of ICG clearance studies of mouse liver by real-time PACT were shown in Fig. 3. Compared with the before injection group, the PA signal had a significant enhancement and changed over time after injection of ICG (Fig. 3A). Quantitative PA signal enhancement curves in the healthy, early and advanced stages of modeling were recorded in Fig. 3B–D, respectively. The control group showed a rapid decrease after the peak point, while the elimination of ICG for the disease groups was much slower. Quantitative T_{max} and $T_{1/2}$ were presented in Fig. 3E and F, respectively. Compared with the control group, the T_{max} of disease models was prolonged (control group, 11.4 ± 2.0 s; early stage, 20.1 ± 1.1 s; advanced stage, 22.8 ± 1.6 s; $P < 0.05$). The $T_{1/2}$ was also slowing down in the disease models (control group, 59.8 ± 4.5 s; early stage, 189.0 ± 9.1 s; advanced stage, 262.6 ± 9.0 s; $P < 0.05$). The results suggested that the metabolism of ICG in liver was related to the degree of HT1 progress, and PAI can be used to in vivo evaluate the liver function reserve.

3.3. Three-dimensional US and PAI of kidneys

Transverse US images revealed the macroscopic morphology of the kidneys with insufficient microscopic detail (Fig. 4A, C). Transverse PACT images exhibited that under the healthy conditions, renal arteries and veins including all of the anterior, superior, inferiory, posterior segment were obvious and continuous. The renal medullas were characterized by a large number of interlobar arteries and veins. However, the vascular structure was damaged and blurred in the early stages of HT1, and became more severe and faded away in the advanced stages. After filtering and then binary processing of the PACT images, the network skeleton of blood vessels could be obtained and the effective BVD was calculated. Fig. 4B shows the BVD of left kidney (control group, 1.2 ± 0.2 mm/mm^2; early stage, 0.6 ± 0.1 mm/mm^2; advanced stage, 0.4 ± 0.1 mm/mm^2; $P < 0.05$), while Fig. 4D gives the BVD value of right kidney (control group, 1.1 ± 0.1 mm/mm^2; early stage, 0.6 ± 0.1 mm/mm^2; advanced stage, 0.3 ± 0.1 mm/mm^2; $P < 0.05$). The BVD gradually decreased as the microvasculature was severely damaged with the progress of HT1.

Fig. 5 shows the US and PACT images of the left kidney (Fig. 5A) and right kidney (Fig. 5C) both in the coronal and sagittal plane. The US images demonstrated the macroscopic morphology of the kidneys. PACT images showed that the hemoglobin content as indicated by the arrows in the kidneys gradually decreased as HT1 progresses. Fig. 5B and D show the averaged PA signals of hemoglobin from left kidney (control group, 6.3 ± 0.9 a.u.; early stage, 3.0 ± 0.3 a.u.; advanced stage, 1.2 ± 0.1 a.u.; $P < 0.05$) and right kidney (control group, 6.8 ± 0.5 a.u.; early stage, 3.4 ± 0.6 a.u.; advanced stage, 1.2 ± 0.3 a.u.; $P < 0.05$), respectively.

Fig. 6 presents the renal surface structure at a much smaller level from the PAM imaging compared with that from PACT. Fig. 6A clearly shows the vascular changes between the healthy and diseased kidney. The capillaries that bend around the renal tubules were found on the surface of the kidney. The smallest microvessel obtained by PAM was about 8 μm in diameter. The microvessels were destroyed, part of them disappear, and the overall distribution became uneven in the disease stages. Fig. 6B shows the binarization of PAM images, and then the percentage of blood vessel area was calculated (control group, 37.1 %; early stage, 21.2 %; advanced stage, 11.9 %). sO_2 of mouse kidney at different stages of modeling was examined in Fig. 6E, and the quantitative levels decreased significantly (control group, 0.91; early stage, 0.79; advanced stage, 0.62).

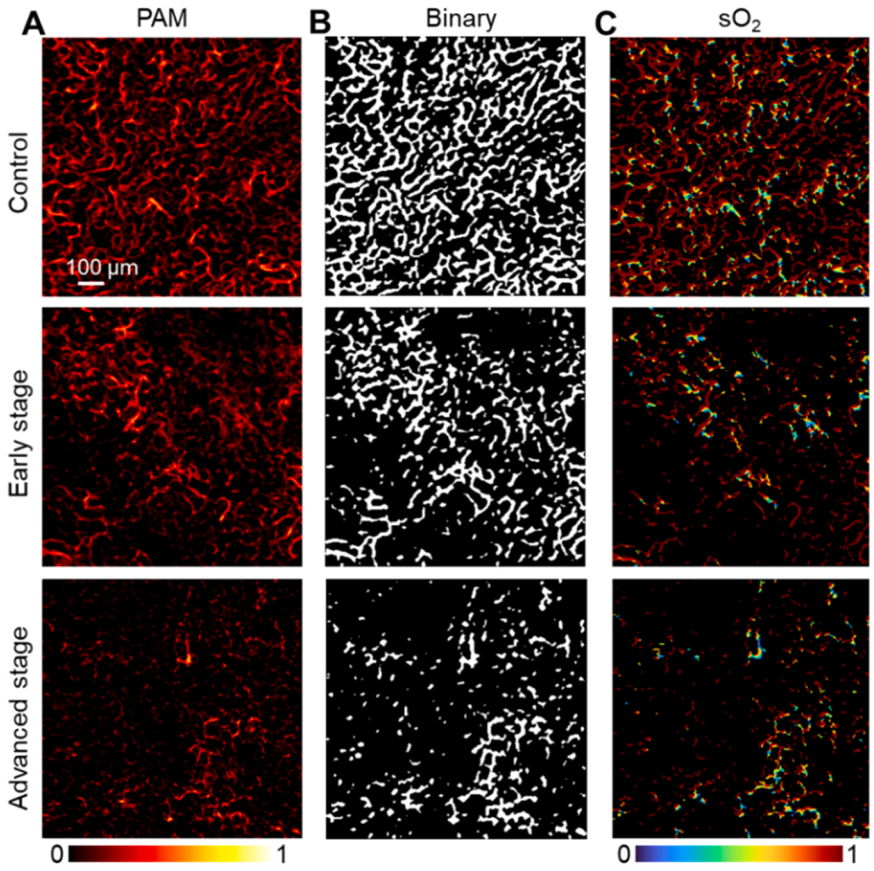

Fig. 6. PAM images of the vessels and sO_2 of mouse kidney at different stages of modeling. A, PAM images. B, Filter and binary processing of PAM images. C, sO_2 of mouse kidney.

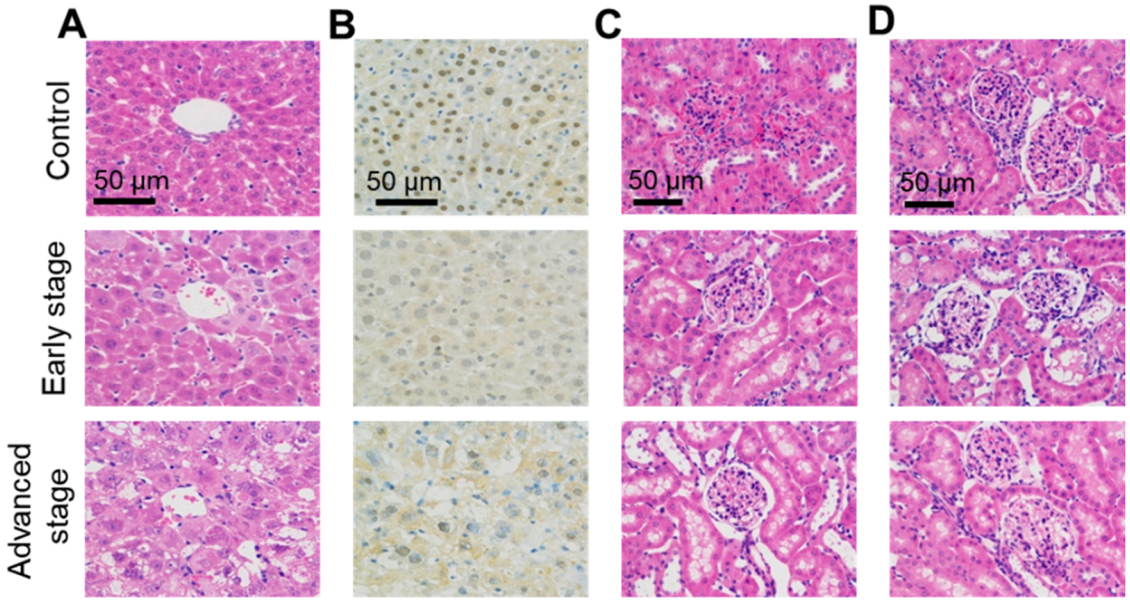

Fig. 7. Pathological examination of the mouse liver and kidney at different stages of modeling. A, H&E staining of mouse liver. B, Immunohistochemical staining of mouse liver. C, H&E staining of left kidney. D, H&E staining of right kidney.

3.4. Pathological examination

H&E staining demonstrated that in the control group, cells arranged closely and orderly, and the cell morphology was full and filled with cytoplasm. In the early stage, the denatured nuclei of hepatocytes were concentrated, and the structure of liver plate disappeared. Ground glass change was observed in the hepatocytes. In the advanced stage, hepatocytes were enlarged in size and had shrunken nuclei with loose cytoplasm. Numerous fat vacuoles could be seen in the cytoplasm, accompanied by a large number of inflammatory cells and cell necrosis

(Fig. 7A). Rabbit anti-mouse FAH antibody and goat rabbit IgG (HRP conjugate) were used for immunohistochemical staining (Fig. 7B), the nuclei of liver samples in the control group showed positive FAH staining, whereas the diseased groups showed no expression. In the HT1 model, both of the left and right kidney tissues appeared a certain degree of damage. H&E staining in Fig. 7C and D showed that in the control group, the structure of kidney tissue was complete, the outline of renal tubules and glomeruli was clear and distinguishable. The structure disappeared, neutrophils, lymphocytes and other inflammatory cells gradually infiltrated in the early stage of HT1. A large number of fat vacuoles and balloon like degeneration appeared in the cytoplasm, accompanied by serious inflammatory and apoptosis in the advanced stage.

4. Discussion and conclusion

Currently, in vivo clinical imaging techniques such as MRI and US are utilized in the study of HT1 to detect the lesions and monitor their development [15–17]. PAI is a promising technique for the high-resolution observation of the microvascular structure and function of liver and kidneys in HT1. As light is absorbed by oxygenated hemoglobin, deoxyhemoglobin or exogenous agents and converted to heat, the subsequent thermoelastic expansion generates an acoustic wave. The morphological characteristics, sO_2 and metabolic capacity can be obtained with a rich optical contrast and high acoustic resolution. This study was carried out to investigate the feasibility of using PAI to perform the structural and functional information, and then provide a new diagnostic basis for imaging compared with clinical conventional imaging methods.

Our results suggested that PAI can uncover diagnostic information of liver and kidney injury and severity in HT1 mouse models. For the structural information of the lesion, PACT can selectively observe the changes of the vessel skeleton in the liver and kidney at the submillimeter scale, while US only gives the overall morphology at the millimeter scale. PAM can present the changes of the hepatic lobule which is the smallest structural unit of liver, and the capillaries that bend around the renal tubules at the micro scale. The results of PAM showed the microvascular network which is up to 8 μm in diameter in the surface of liver and kidney at the microscopic level. For the function monitoring, PACT can observe the changes of the hemoglobin content in vivo during the course of HT1. With the aid of exogenous contrast agent ICG, liver function reserve was successfully evaluated by PACT. The results exhibited that T_{max} and $T_{1/2}$ of ICG metabolic capacity of liver during the HT progression. As previous studies indicating, ICG enters into hepatic sinuses after intravenous injection, is efficiently absorbed by hepatocytes, and undergoes exponential concentration reduction, as it is secreted into bile rapidly, without secondary absorption occurring under normal healthy circumstances [42]. In the liver fibrosis model, T_{max} of advanced stage group (8 weeks) is 11.6 times larger than that of control group (9 s vs 104 s), while $T_{1/2}$is 11.4 times (28 s vs 318 s). In the HT1 model, both T_{max} (11.4 s vs 22.8 s) and $T_{1/2}$ (59.8 s vs 262.6 s) are prolonged in the control and advanced stages, respectively. It can be concluded that HT1 mainly restricted the elimination of ICG, while fibrosis has a greater effect on liver clearance of ICG than HT1. The large amount of extracellular matrix deposition, hepatocyte necrosis and apoptosis which were observed in pathological examination would account for the inhibition of ICG uptake and excretion in HT1. Taking advantage of the optical absorption difference of endogenous oxygenated hemoglobin and deoxyhemoglobin, PAM depicted the sO_2 profile on a micro-scale.

Oxygenation depends on a balance between vascular blood flow and oxygen consumption, which finally results in the vascular injury and the loss of hepatic and renal function. The use of noninvasive PAI to monitor the vascular changes and dysfunction of liver disease or renal tubular in HT could complement conventional US measurement since the vasculature has been implicated in playing a role in hepatic and renal function. US imaging is based on differences in tissue acoustic impedance and provides only limited information in the diagnosis of HT1. In contrast, it is exciting to note that PAI basing on the optical absorption properties of tissues, showed great advantages in monitoring the surface microstructure of liver and kidneys at the micron scale, which is very helpful for the accurate diagnose. In the clinic, liver transplantation would be performed for those who have severe liver failure and fail to respond to nitisinone therapy or have documented evidence of malignant changes in hepatic tissue [48]. Fittingly, PAI has provided an in vivo assessment method for liver function reserve, which could guide the operation of liver transplantation. Pathological examination confirmed that many cells undergo necrosis, which is consistent with the previous studies that acute accumulation of fumarylacetoacetic acid triggers apoptosis in both hepatocytes and renal tubular cells [49,50]. Cell death would further lead to the vascular damage and dysfunction of liver and kidneys.

Several limitations exist in this study. First, due to the limited imaging depth, only the surface microvascular information (usually less than 200 μm in depth) can be clearly obtained. However, deeper vascular lesions play an important role in the diagnosis and treatment of HT1. As human liver and kidney are posed in 15-cm depth, the imaging setup used in this study will not be sufficient and PA endoscopy will be of great use for clinical HT1 diagnostics after making a small hole in the abdomen. Second, the staging of tyrosinemia lacked strict criteria in this study. Different degrees of disease model in HT1 should be considered and relative modeling method should be established for further validation. How to match the microstructural and metabolic capabilities based on PAI with US or MRI, as well as in vitro molecular biomarker testing, is a key question, which restricts the clinical translation of PAI for clinical HT1 diagnostics. Third, large population of prospective preclinical and clinical study should be performed in the future. Regulatory red tapes by regulatory authorities present one of the challenges in translating PAI to the clinics. At present, only imagio Breast Imaging System by Seno Medical Instruments, Inc has been approved by FDA. To accelerate the application of photoacoustic imaging in the diagnosis of HT, more PAI systems need to be approved for clinical use in the future.

In summary, using cross-scale PAI to quantitatively monitor the liver and kidney lesions in HT1 is a safe, versatile and effective method for characterizing vascular structure, blood oxygen function, and liver reserve assessment during the progression of HT1. PAM with a high frequency transducer is more suitable for microstructure visualization, while PACT with a low frequency transducer is recommended for deep lesion detection and metabolic level monitoring. PAI has provided the structural and functional information on a cross-scale, and is potentially promising for clinical diagnosis of HTI in a new perspective.

Declaration of Competing Interest

The authors declare that they have no known competing financial interests or personal relationships that could have appeared to influence the work reported in this paper.

Data Availability

Data will be made available on request.

Acknowledgements

This work was supported by National Natural Science Foundation of China (11664011) and Guangdong Provincial People's Hospital Supporting Fund for Talent Program (KJ012020638).

References

[1] P.A. Russo, G.A. Mitchell, R.M. Tanguay, Tyrosinemia: a review, Pediatr. Dev. Pathol. 4 (3) (2001) 212–221.

[2] B. Lindblad, S. Lindstedt, G. Steen, On the enzymic defects in hereditary tyrosinemia, Proc. Natl. Acad. Sci. USA 74 (10) (1977) 4641–4645.

[3] R.M. Tanguay, J.P. Valet, A. Lescault, J.L. Duband, M. Plante, Different molecular basis for fumarylacetoacetate hydrolase deficiency in the two clinical forms of hereditary tyrosinemia (type I), Am. J. Hum. Genet. 47 (2) (1990) 308–316.

[4] J.M. Chinsky, R. Singh, C. Ficicioglu, C.D.M. van Karnebeek, M. Grompe, G. Mitchell, S.E. Waisbren, M. Gucsavas-Calikoglu, M.P. Wasserstein, K. Coakley, C. R. Scott, Diagnosis and treatment of tyrosinemia type I: a US and Canadian consensus group review and recommendations, Genet. Med. 19 (12) (2017) (1380-1380).

[5] C.J.L. Koelink, P. van Hasselt, A.D. Ploeg, M.M. van den Heuvel-Elbrink, F. A. Wijburg, C.M.A. Bijleveld, F.J. van Spronsen, Tyrosinernia type I treated by NTBC: how does AFP predict liver cancer? Mol. Genet. Metab. 89 (4) (2006) 310–315.

[6] M. Almuqbil, J. Knoll, J.M. Chinsky, Late development of hepatocellular carcinoma in tyrosinemia type 1 despite nitisinone (NTBC) treatment, J. Pediatr. Gastroenterol. Nutr. 71 (2) (2020) e73–e75.

[7] E. Holme, S. Lindstedt, Nontransplant treatment of tyrosinemia, Clin. Liver Dis. 4 (4) (2000) 805–814.

[8] D.A. Schady, A. Roy, M.J. Finegold, Liver tumors in children with metabolic disorders, Transl. Pediatr. 4 (4) (2015) 290–303.

[9] A. Maiorana, M. Malamisura, F. Emma, S. Boenzi, V.M. Di Ciommo, C. Dionisi-Vici, Early effect of NTBC on renal tubular dysfunction in hereditary tyrosinemia type 1, Mol. Genet. Metab. 113 (3) (2014) 188–193.

[10] A.M. Das, Clinical utility of nitisinone for the treatment of hereditary tyrosinemia type-1 (HT-1), Appl. Clin. Genet. 10 (2017) 43–48.

[11] M. Grompe, M. St-Louis, S.I. Demers, M. Al-Dhalimy, B. Leclerc, R.M. Tanguay, A single mutation of the fumarylacetoacetate hydrolase gene in French Canadians with hereditary tyrosinemia type I, N. Engl. J. Med. 331 (6) (1994) 353–357.

[12] J. Poudrier, F. Lettre, C.R. Scriver, J. Larochelle, R.M. Tanguay, Different clinical forms of hereditary tyrosinemia (type I) in patients with identical genotypes, Mol. Genet. Metab. 64 (2) (1998) 119–125.

[13] M. Ashorn, S. Pitkanen, M.K. Salo, M. Heikinheimo, Current strategies for the treatment of hereditary tyrosinemia type I, Paediatr. Drugs 8 (1) (2006) 47–54.

[14] M. Iavarone, M. Vigano, N. Piazza, V. Occhipinti, A. Sangiovanni, M. Maggioni, G. D'Ambrosio, L.V. Forzenigo, F. Motta, P. Lampertico, M.G. Rumi, M. Colombo, Contrast imaging techniques to diagnose hepatocellular carcinoma in cirrhotics outside regular surveillance, Ann. Hepatol. 18 (2) (2019) 318–324.

[15] G.C. Mueller, H.K. Hussain, R.C. Carlos, H.V. Nghiem, I.R. Francis, Effectiveness of MR imaging in characterizing small hepatic lesions: routine versus expert interpretation, Ajr Am. J. Roentgenol. 180 (2003) 673–680.

[16] P.N. Rao, Nodule in liver: investigations, differential diagnosis and follow-up, J. Clin. Exp. Hepatol. 4 (Suppl. 3) (2014) S57–S62.

[17] Z. Wu, F. Duan, J. Zhang, S. Li, L. Nie, In vivo dual-scale photoacoustic surveillance and assessment of burn healing, Biomed. Opt. Express 10 (7) (2019) 3425.

[18] T.R. Zhao, A.E. Desjardins, S. Ourselin, T. Vercauteren, W.F. Xia, Minimally invasive photoacoustic imaging: current status and future perspectives, Photoacoustics 16 (2019), 100146.

[19] P.K. Upputuri, M. Pramanik, Photoacoustic imaging in the second near-infrared window: a review, J. Biomed. Opt. 24 (4) (2019), 040901.

[20] D. Cui, Y. Shi, D. Xing, S. Yang, Ultrahigh sensitive and tumor-specific photoacoustography in NIR-II region: optical writing and redox-responsive graphic fixing by AgBr@PLGA nanocrystals, Nano Lett. 21 (16) (2021) 6914–6922.

[21] L.V. Wang, J. Yao, A practical guide to photoacoustic tomography in the life sciences, Nat. Methods 13 (8) (2016) 627–638.

[22] M. Visscher, M.A. Pleitez, K. Van Gaalen, I.M. Nieuwenhuizen-Bakker, V. Ntziachristos, G. Van Soest, Label-free analytic histology of carotid atherosclerosis by mid-infrared optoacoustic microscopy, Photoacoustics 26 (2022), 100354.

[23] S. Park, F.J. Brooks, U. Villa, R. Su, M.A. Anastasio, A.A. Oraevsky, Normalization of optical fluence distribution for three-dimensional functional optoacoustic tomography of the breast, J. Biomed. Opt. 27 (3) (2022), 036001.

[24] M.Y. Lucero, J. Chan, Photoacoustic imaging of elevated glutathione in models of lung cancer for companion diagnostic applications, Nat. Chem. 13 (12) (2021) 1248–1256.

[25] J. Weber, P.C. Beard, S.E. Bohndiek, Contrast agents for molecular photoacoustic imaging, Nat. Methods 13 (8) (2016) 639–650.

[26] A.B.E. Attia, G. Balasundaram, M. Moothanchery, U.S. Dinish, R.Z. Bi, V. Ntziachristos, M. Olivo, A review of clinical photoacoustic imaging: current and future trends, Photoacoustics 16 (2019), 100144.

[27] L. Lin, L.V. Wang, The emerging role of photoacoustic imaging in clinical oncology, Nat. Rev. Clin. Oncol. 19 (6) (2022) 365–384.

[28] J. Zhou, J.V. Jokerst, Photoacoustic imaging with fiber optic technology: a review, Photoacoustics 20 (2020), 100211.

[29] W. Li, U.A.T. Hofmann, J. Rebling, Q. Zhou, Z. Chen, A. Ozbek, Y. Gong, P. Subochev, D. Razansky, X.L. Dean-Ben, Broadband model-based optoacoustic mesoscopy enables deep-tissue imaging beyond the acoustic diffraction limit, Laser Photonics Rev. 16 (5) (2022), 2100381.

[30] A. Sun, Y. Ji, Y. Li, W. Xie, Z. Liu, T. Li, T. Jin, W. Qi, K. Li, C. Wu, L. Xi, Multicolor photoacoustic volumetric imaging of subcellular structures, ACS Nano 16 (2) (2022) 3231–3238.

[31] J.M. Jeon, J. Kim, C. Kim, Multiplane spectroscopic whole-body photoacoustic imaging of small animals in vivo, Med. Biol. Eng. Comput. 54 (2) (2016) 283–294.

[32] L. Li, S. Li, Z. Fan, G. Huang, J. Tang, L. Nie, Current strategies of photoacoustic imaging assisted cancer theragnostics toward clinical studies, ACS Photonics 9 (8) (2022) 2555–2578.

[33] O. Ogunlade, J.J. Connell, J.L. Huang, E. Zhang, M.F. Lythgoe, D.A. Long, P. Beard, In vivo three-dimensional photoacoustic imaging of the renal vasculature in preclinical rodent models, Am. J. Physiol.-Ren. Physiol. 314 (6) (2018) F1145–F1153.

[34] M.Y. Lucero, Y. Tang, C.J. Zhang, S. Su, J.A. Forzano, V. Garcia, X. Huang, D. Moreno, J. Chan, Activity-based photoacoustic probe for biopsy-free assessment of copper in murine models of Wilson's disease and liver metastasis, Proc. Natl. Acad. Sci. USA 118 (36) (2021), e2106943118.

[35] C. Zhang, Z. Qiu, L. Zhang, S. Wang, S. Zhao, Q. Pang, H. Liang, Mitochondria-targeted fluorescence/photoacoustic dual-modality imaging probe tailored for visual precise diagnosis of drug-induced liver injury, Anal. Chem. 94 (16) (2022) 6251–6260.

[36] H. Deng, W. Shang, K. Wang, K. Guo, Y. Liu, J. Tian, C. Fang, Targeted-detection and sequential-treatment of small hepatocellular carcinoma in the complex liver environment by GPC-3-targeted nanoparticles, J. Nanobiotechnol. 20 (1) (2022) 156.

[37] Y. Zhou, P. Li, X. Wang, C. Wu, N. Fan, X. Liu, L. Wu, W. Zhang, W. Zhang, Z. Liu, B. Tang, In situ visualization of peroxisomal viscosity in the liver of mice with non-alcoholic fatty liver disease by near-infrared fluorescence and photoacoustic imaging, Chem. Sci. 11 (44) (2020) 12149–12156.

[38] E. Hysi, X. He, M.N. Fadhel, T. Zhang, A. Krizova, M. Ordon, M. Farcas, K.T. Pace, V. Mintsopoulos, W.L. Lee, M.C. Kolios, D.A. Yuen, Photoacoustic imaging of kidney fibrosis for assessing pretransplant organ quality, JCI Insight 5 (10) (2020), e136995.

[39] T.T. Qiu, J.G. Yang, T. Pan, C.H. Peng, H.B. Jiang, Y. Luo, Assessment of liver function reserve by photoacoustic tomography: a feasibility study, Biomed. Opt. Express 11 (7) (2020) 3985–3995.

[40] W. Zhang, Z. Shen, Y. Wu, W. Zhang, T. Zhang, B.Y. Yu, X. Zheng, J. Tian, Renal-clearable and biodegradable black phosphorus quantum dots for photoacoustic imaging of kidney dysfunction, Anal. Chim. Acta 1204 (2022), 339737.

[41] T. Guan, W. Shang, H. Li, X. Yang, C. Fang, J. Tian, K. Wang, From detection to resection: photoacoustic tomography and surgery guidance with indocyanine green loaded gold nanorod@liposome core–shell nanoparticles in liver cancer, Bioconjug. Chem. 28 (4) (2017) 1221–1228.

[42] J. Lv, Y. Xu, L. Xu, L. Nie, Quantitative functional evaluation of liver fibrosis in mice with dynamic contrast-enhanced photoacoustic imaging, Radiology 300 (1) (2021) 89–97.

[43] Q. Yu, S. Huang, Z. Wu, J. Zheng, X. Chen, L. Nie, Label-free visualization of early cancer hepatic micrometastasis and intraoperative image-guided surgery by photoacoustic imaging, J. Nucl. Med. 61 (7) (2020) 1079–1085.

[44] Q. Li, K. Chen, W. Huang, H. Ma, X. Zhao, J. Zhang, Y. Zhang, C. Fang, L. Nie, Minimally invasive photothermal ablation assisted by laparoscopy as an effective preoperative neoadjuvant treatment for orthotopic hepatocellular carcinoma, Cancer Lett. 496 (2021) 169–178.

[45] J. Yang, G. Zhang, W. Chang, Z. Chi, Q. Shang, M. Wu, T. Pan, L. Huang, H. Jiang, Photoacoustic imaging of hemodynamic changes in forearm skeletal muscle during cuff occlusion, Biomed. Opt. Express 11 (8) (2020) 4560–4570.

[46] S. Saito, Y. Moriyama, S. Kobayashi, R. Ogihara, D. Koto, A. Kitamura, T. Matsushita, M. Nishiura, K. Murase, Assessment of liver function in thioacetamide-induced rat acute liver injury using an empirical mathematical model and dynamic contrast-enhanced MRI with Gd-EOB-DTPA, J. Magn. Reson. Imaging 36 (6) (2012) 1483–1489.

[47] M.S. Hassouna, A.A. Farag, Multistencils fast marching methods: a highly accurate solution to the eikonal equation on Cartesian domains, IEEE Trans. Pattern Anal. Mach. Intell. 29 (9) (2007) 1563–1574.

[48] D.C. Bartlett, C. Lloyd, P.J. McKiernan, P.N. Newsome, Early nitisinone treatment reduces the need for liver transplantation in children with tyrosinaemia type 1 and improves post-transplant renal function, J. Inherit. Metab. Dis. 37 (5) (2014) 745–752.

[49] S. Kubo, M. Sun, M. Miyahara, K. Umeyama, K.-I. Urakami, T. Yamamoto, C. Jakobs, I. Matsuda, F. Endo, Hepatocyte injury in tyrosinemia type 1 is induced by fumarylacetoacetate and is inhibited by caspase inhibitors, Proc. Natl. Acad. Sci. USA 95 (16) (1998) 9552–9557.

[50] M.S. Sun, S. Hattori, S. Kubo, H. Awata, I. Matsuda, F. Endo, A mouse model of renal tubular injury of tyrosinemia type 1: development of de Toni Fanconi syndrome and apoptosis of renal tubular cells in Fah/Hpd double mutant mice, J. Am. Soc. Nephrol. 11 (2) (2000) 291–300.

Guojia Huang is currently an associate research fellow of Research Center of Medical Sciences of Guangdong Provincial People's Hospital, Guangdong Academy of Medical Sciences. He got his Ph.D. degree from Sun Yat-sen University, Guangzhou, China in 2015. His research interests are the development optical and photoacoustic imaging technology and their clinical application.

Jing Lv is currently a postdoctoral fellow of Research Center of Medical Sciences of Guangdong Provincial People's Hospital, Guangdong Academy of Medical Sciences. She got his Ph.D. degree from Xiamen University, China in 2022. Her main research interests are the structural and functional photoacoustic imaging application of cardiovascular and cerebrovascular disease models as well as contrast-enhanced quantitative, dynamic, metabolic imaging of livers and kidneys.

Yong He is a master's student at Guangdong University of Technology. His research interests are in the development of photoacoustic imaging systems for medical applications.

Jian Yang is a director doctor of the Hepatobiliary Surgery (I) in Zhujiang Hospital, Southern Medical University, and doctoral supervisor. He has been working on the application of digital intelligent diagnosis and treatment technology in the hepatobiliary and pancreatic surgical diseases, and the digital minimally invasive treatment of the liver and the pancreas.

Lvming Zeng is currently an associate researcher of the State Key Laboratory of Precision Electronic Manufacturing Technology and Equipment, Guangdong University of Technology. He received the M.S. degree in optics from South China Normal University, Guangzhou, China, in 2007. His current research focuses on the applications of laser ultrasound in biomedical imaging and industry inspection.

Liming Nie is a professor and Ph.D. supervisor at Research Center of Medical Sciences of Guangdong Provincial People's Hospital, Guangdong Academy of Medical Sciences. His laboratory focuses on optical imaging technology, mainly on photoacoustic microscopy, photoacoustic computed tomography, and other related imaging modalities. One of his aims is to provide effective and low-cost imaging instruments for disease diagnosis and treatment monitoring.